Check for updates

ANNUAL ISSUE

**EARLY CAREER SCHOLARS IN MATERIALS SCIENCE, 2024**

# Outlook on texture evolution in additively manufactured stainless steels: Prospects for hydrogen embrittlement resistance, overview of mechanical, and solidification behavior

Saket Thapliyal[1,a)] ⓘ, Jiahao Cheng[1,a)], Jason Mayeur[1,a)], Yukinori Yamamoto[2], Patxi Fernandez-Zelaia[1], Andrzej Nycz[1], Michael M. Kirka[1]

[1] *Manufacturing Science Division, Oak Ridge National Laboratory, Oak Ridge, TN, USA*
[2] *Materials Science and Technology Division, Oak Ridge National Laboratory, Oak Ridge, TN, USA*
[a)] Address all correspondence to these authors. e-mails: thapliyals@ornl.gov; chengj@ornl.gov; mayeurjr@ornl.gov

Realizing application specific manufacture with fusion-based additive manufacturing (F-BAM) processes requires understanding of the physical phenomena that drive evolution of microstructural attributes, such as texture. Current approaches for understanding texture evolution in F-BAM are majorly considerate of the phenomena occurring only during solidification. This hinders the comprehensive understanding and control of texture during F-BAM. In this perspective article, we discuss several physical phenomena occurring during and after solidification that can determine texture in F-BAM processed stainless steels (SS). A crystal plasticity-coupled hydrogen adsorption-diffusion modeling framework is also leveraged to demonstrate the prospects of grain boundary engineering with F-BAM for enhanced hydrogen embrittlement resistance of SS. Implications of varying thermokinetics in F-BAM for solidification behavior of SS are discussed. Additionally, microstructural attributes that are key to high temperature mechanical performance of SS are highlighted. Considerations as outlined in this perspective article will enable grain boundary engineering and application specific microstructural design of SS with F-BAM.

Saket Thapliyal is a Materials Scientist: R&D Associate staff member at the Manufacturing Demonstration Facility in Oak Ridge National Laboratory. Saket received his Ph.D. in Materials Science and Engineering at the University of North Texas. He received his M.S. in Mechanical Engineering at the University of Texas at Arlington and his B. Tech in Mechanical Engineering at the Uttarakhand Technical University, India. The overarching goal of Saket's current research is to establish *chemistry-processing-structure-properties* relationships in fusion-based additive manufacturing (AM) of steels and refractory alloys. Particularly, Saket investigates the effect of alloy chemistry on the solidification behavior, fusion AM processability, microstructural evolution, and mechanical behavior of novel and conventional alloys, including high entropy alloys, ferrous and non-ferrous alloys. Additionally, he is interested in designing alloys and

Saket Thapliyal

microstructures for extreme environments, such as high temperature environments, hydrogen-rich environments, and high radiation environments using fusion AM. Saket's previous research focused on designing Al alloys, ferrous high entropy alloys, and steels for fusion AM using CALPHAD tools and experimental methods. This research led to the development of a novel two-pronged approach that involved heterogeneous nucleation and eutectic solidification for designing hot cracking-resistant high performance alloys for fusion-based AM processes.

## Introduction

Fusion-based additive manufacturing (F-BAM) processes, such as laser-powder bed fusion (L-PBF), electron beam-powder bed fusion and directed energy deposition (DED) have evolved from rapid prototyping processes to being integral to the contemporary manufacturing supply chain networks. At the inception, while the capabilities of F-BAM were demonstrated through processing of legacy alloys, like SS316, Ti–6Al–4V, and Ni- and Co-based superalloys, retrospectively, the evolution of F-BAM also required successful demonstration of *processability* and *properties* of the alloys that are designed specifically for F-BAM. Such demonstration highlights the endeavors towards understanding the process dynamics involved in F-BAM. Note that the term '*process dynamics*' is specifically used to represent the thermokinetics and the overall physical phenomena that may determine the microstructural evolution during the process [1–4]. Thermokinetics are usually represented by thermal gradients (G), solid–liquid interface velocity (also called growth rates, R), and/or other parameters derived from G and R, such as cooling rate ($G \times R$) and G/R. Furthermore, for disruptive processing technologies, such as F-BAM, a process specific alloy design facilitates application specific manufacture and a widespread implementation of such processing technologies [5]. Elaborating, the physical phenomena differ from one manufacturing process to the other, and so do the microstructural hierarchy and heterogeneity and the ensuing mechanical behavior of the processed alloy. e.g., depending on the thermokinetics during processing, the fraction of martensite phase may vary in the precipitation hardenable (PH) 17–4 stainless steels (SS), i.e., the conventionally processed 17–4 PH SS may exhibit martensite-dominant microstructure, whereas its F-BAM processed counterpart may exhibit a large fraction of retained austenite phase [6]. Subsequently, the mechanical behavior of the conventionally processed component may vary substantially from its F-BAM processed counterpart. Therefore, achieving the control of microstructural attributes and the required mechanical properties either through alloy design or F-BAM process parameters requires understanding of the physical phenomena involved during F-BAM [7, 8].

While steels are ubiquitous in structural applications, and SS were one of the first few legacy alloys that were processed with F-BAM processes, controlling the solidification behavior and microstructural attributes, such as texture and phase transformation in these class of alloys during F-BAM processing remain challenging. As such, the control of solidification pathway/modes, e.g., completely austenitic, δ-ferritic to austenitic (FA), and austenitic to ferritic (AF), in F-BAM processed steels is still difficult to achieve. Notably, solidification modes can affect the cracking susceptibility, the phases present within the processed alloys, and the ensuing properties [9, 10]. Furthermore, although the evolution of crystallographic texture stems from an interplay of multiple physical phenomena [1, 11], a knowledge gap becomes evident when the current endeavors towards understanding the texture evolution in F-BAM processed steels remain considerate of only a few physical phenomena, such as competitive growth and epitaxial growth [12, 13]. Considering that crystallographic texture determines the mechanical behavior of steels irrespective of their stacking fault energies (SFE), i.e., high, moderate, or low SFE steels, such knowledge gap is inhibitory for a widespread implementation of F-BAM in structural applications [14–18]. Note that the SFE has been invoked here because it determines if the plastic deformation occurs majorly through dislocation slip, twinning, or deformation induced phase transformations; crystallographic texture affects all these deformation mechanisms in steels. In addition to determining the room temperature mechanical behavior, crystallographic texture determines the mechanical behavior of steels under harsh environments, e.g., hydrogen-rich environments and elevated temperatures [19, 20]. With the world at the verge of climate crisis, the manufacturing industry has witnessed an unprecedented push for adopting environmentally sustainable energy resources and energy efficient structures. Considering the ubiquity of steels in structural applications, such adoption necessitates designing '*future-proof*' steels, i.e., steels that are compatible with environmentally sustainable energy resources like hydrogen, and implementing environmentally sustainable processing routes for processing steels [21]. Although F-BAM can facilitate a sustainable processing of '*future-proof*' steels, such an implementation of F-BAM must enable design of hydrogen embrittlement (HE)-resistant steels. The microstructural attributes that affect the HE resistance of steels include texture, grain boundaries, and primary and secondary phases [22–24]. Furthermore, considering that one of the core capabilities of F-BAM is manufacturing geometrically complex components, such as turbine blades that are operative at elevated temperatures, an enhanced efficiency of modern power plants can be attained through manufacture of steels with high temperature-resistant microstructure. Therefore,

understanding the mechanisms behind texture evolution and delineating the evolution of distinct aspects of microstructural attributes during F-BAM is imperative for facilitating a widespread and long-lasting implementation of F-BAM in structural applications.

In this perspective article, we delineate the current knowledge gaps in understanding the solidification behavior and the mechanisms behind evolution of several microstructural attributes, such as texture, and phases during F-BAM of SS. In order to maintain conciseness and due to the significance of SS as HE-resistant structural materials, this article focuses only on SS. Possible underlying phenomena determining texture evolution during F-BAM are discussed in detail. Furthermore, examples from experimental and computational investigations are provided to highlight noteworthy effects of these phenomena on texture evolution during F-BAM. We also highlight the prospects of using F-BAM processes for designing SS with a HE- and high temperature-resistant microstructure. A perspective on the use of coupled computational models for investigating the interaction between hydrogen and F-BAM produced microstructure is also provided with example. Such models can facilitate design of SS with hydrogen-resistant microstructures with F-BAM. Implications of microstructural attributes of F-BAM processed SS on their high-temperature mechanical behavior are also discussed.

## Overcoming knowledge gaps in texture evolution during F-BAM: prospects for mechanical properties and HE resistance of SS

### Overcoming the knowledge gaps inhibiting texture control with F-BAM

The effect of crystallographic texture on mechanical behavior of F-BAM processed steels has been widely reported [25]. A Schmid factor-based analysis readily reveals the effect of crystallographic texture on plastic deformation behavior, including dislocation slip, deformation twinning, and deformation induced phase transformation behavior [14, 15, 26, 27]. Despite the widely acknowledged effect of crystallographic texture on mechanical behavior, majorly, only a few mechanisms, such as competitive and epitaxial growth occurring during solidification, have been invoked to elucidate the texture evolution in F-BAM processed SS. Notably, a comprehensive understanding and control of texture evolution in F-BAM engenders consideration of mechanisms that govern the selection of both—primary and secondary crystallographic orientations. By the term 'primary orientations', we mean the crystallographic orientation in the build direction (BD). Similarly, the term 'secondary orientations' must not be confused with the orientations of secondary

dendritic arms, instead, it means the crystallographic orientations in the plane orthogonal to the BD. In this article, we adhere to only two secondary orientations in the plane orthogonal to the BD—one in the scanning direction (SD) and the other along normal to the SD, termed as transverse direction (TD). The type of secondary orientation (SD or TD) under consideration will be explicitly mentioned.

For cubic crystals, competitive growth leads to the alignment of <001> directions along the maximum thermal gradient vector (often perpendicular to the melt pool boundaries). The elastically soft <001> directions in cubic crystals are directions of easy growth during solidification. Consequently, crystals that have their <001> directions aligned along the direction of maximum thermal gradient (normal to the melt pool boundary), 'outgrow' the non-aligned crystals. The key point to note here is that such crystal growth does not constrain crystal rotation about normal direction to the melt pool boundary, and thus, it does not determine the overall crystallographic texture. Depending on the melt pool shape, multiple primary orientations may result from competitive growth driven crystallographic growth. An example of such unconstrained crystallographic rotation (about normal direction to the melt pool boundary) despite competitive growth is provided in Fig. 1(a) and (b). The electron backscatter diffraction (EBSD) inverse pole figure (IPF) orientation maps shown here were acquired from a melt pool of wire-arc additive manufacturing (WAAM)-processed SS316L. The primary crystallographic orientations are shown in Fig. 1(a), whereas Fig. 1(b) shows the secondary crystallographic orientations along the SD. The crystal orientation in regions 1 and 2 in the IPF maps are illustrated in Fig. 1(c) and (d), respectively where the red arrows point towards the heat extraction direction during solidification, i.e., the direction opposite to the maximum thermal gradients normal to the melt pool boundary. Note that the crystal orientation as illustrated in Fig. 1(c) and (d) are only few of several possible orientations that can facilitate competitive growth. Evidently, crystals can acquire different primary and secondary orientations even though their <001> directions remain oriented in the direction of maximum thermal gradients. Therefore, controlling the factors that affect *competitive growth* mechanism alone may not facilitate a comprehensive control of crystallographic texture in F-BAM. As for the *epitaxial growth* based arguments, although these can be used for rationalizing the selection mechanism for secondary orientations, they do not elucidate why a single-crystal like texture develops on a polycrystalline substrate and/or previously deposited polycrystalline layers during F-BAM [28, 29]. In light of these arguments, it becomes clear that mechanisms other than competitive growth and epitaxial growth must be operative and need to be investigated for a comprehensive understanding and control of texture in F-BAM.
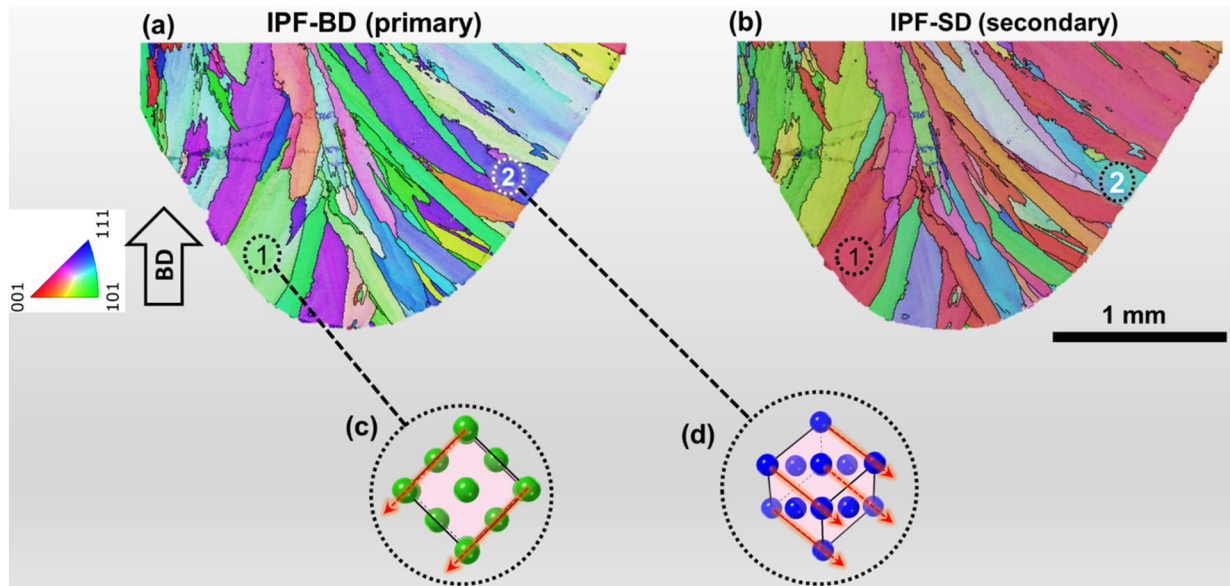
**Figure 1:** EBSD IPF maps illustrating how competitive growth alone may not constrain the primary and secondary crystallographic orientations during F-BAM. EBSD IPF maps along (a) BD depicting primary orientation and (b) SD depicting secondary orientations within a melt pool of WAAM processed SS316L. Illustrations depicting heat extraction direction (indicated by red dashed arrows) and orientations of crystals in regions (c) 1 and (d) 2 from the melt pool.

To date, studies investigating texture evolution in F-BAM processed austenitic steels have widely overlooked the physical phenomena affecting the selection mechanisms for secondary orientations. The significance of understanding the selection mechanism for secondary orientation becomes prominently highlighted when a single crystal (SX)-like texture, i.e., a uniform alignment of primary and secondary crystallographic orientations across the analyzed specimen is reported in F-BAM processed austenitic SS [Fig. 2(a)] [12, 13]. On one hand, obtaining such SX-like texture is encouraging, in that it demonstrates the capability of F-BAM of producing application specific microstructure [30], on the other hand, an incomplete assessment of mechanisms leading to such a uniform alignment of both primary and secondary orientations inhibits the on-demand engineering of such microstructural attributes. As noted earlier, the arguments of competitive growth and epitaxial growth are insufficient for rationalizing the uniform alignment of secondary orientations in such SX-like textured SS deposited on a polycrystalline substrate. In addition, if competitive growth were also to drive the uniform alignment of secondary orientations along the <010> directions in the plane orthogonal to the BD, then the direction of columnar grain growth (meaning the major axis of a growing cell/dendrite) would reside in this orthogonal plane and would not be along the normal direction to the melt pool boundary. However, F-BAM processes resemble directional solidification processes, in that the thermal gradients along one of the directions, generally normal to the melt pool boundary, are highly dominant as compared to the gradients in other directions;
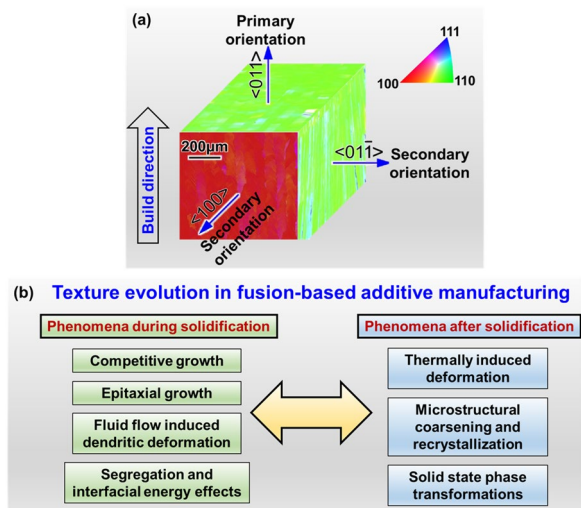


**Figure 2:** Texture evolution in F-BAM processes. (a) A SX like texture in an F-BAM processed SS316L alloy (adapted from [12]). (b) Factors affecting texture evolution during F-BAM processes have been categorized under phenomena occurring *during* and *after* solidification. The yellow double-headed arrow depicts that texture evolution during F-BAM processing is an interplay of multiple physical phenomena occurring during and/or after solidification.

this leads to columnar grain growth along the normal direction to the melt pool boundary as opposed to grain growth in the plane orthogonal to the BD. Such columnar grain growth is evident in Fig. 1(a) and (b). Furthermore, microstructural characterization of F-BAM processed SX-like textured austenitic SS also corroborates that columnar grain growth majorly occurs along the normal direction to the melt pool boundary

[12, 13]. For assessing the texture evolution in steels during F-BAM, although the current investigations have focused on the physical phenomena occurring only during solidification, various physical phenomena occurring during and after solidification may determine the texture during F-BAM processing [1, 3, 31–33]. Figure 2(b) outlines the phenomena from both the categories, i.e., phenomena occurring during and after solidification. Note that the interplay of physical phenomena from within a category or from two different categories may determine the crystallographic texture. It is also worth noting that each of these phenomena can independently determine texture, i.e., even if one of these phenomena subsides under specific F-BAM processing conditions, other phenomena/phenomenon can still affect crystallographic texture. Consideration of multiple physical phenomena and their interplay will facilitate an improved understanding of texture evolution during F-BAM and subsequently allow a repeatable control of texture in F-BAM processed alloys. Next, we discuss the physical phenomena outlined in Fig. 2(b), their origin, and their effect on crystallographic texture in F-BAM. The phenomena discussed here are generally applicable across the classes of alloys.

During solidification, in addition to the competitive and epitaxial growth, dendritic deformation due to fluid flow can affect the crystallographic orientation. Surface tension driven fluid flow towards the cooler regions of the melt pool is prominent during F-BAM processing and leads to Marangoni eddies. For F-BAM processes that are marked by highly undercooled melts, a notable dendritic bending may occur due to fluid flow [34]. Furthermore, in WAAM, in addition to the Marangoni eddies, electromagnetic forces, such as Lorentz force imposed due to the arc may lead to the dendritic deformation. In welding, such fluid flow due to electromagnetic forces is known to occur in opposite direction as compared to the Marangoni convection driven fluid flow [36]. Considering the finer microstructural features in F-BAM due to high cooling rates, a significant deformation of cellular/dendritic arms may occur during solidification and consequently alter the crystallographic texture within the final component.

Solute segregation is prevalent in F-BAM microstructures and leads to reduced interfacial energy due to Gibbsian adsorption [8]. Considering that reducing the interfacial energy is the driving force for grain growth, segregation may hinder grain growth. In case of the competitively growing crystals with <001> aligned along the maximum thermal gradient direction, such reduced growth rates mean that other 'non-aligned' crystals can grow during solidification and can alter the final texture. Solute segregation induced alteration of interfacial energy can also affect the coarsening and recrystallization kinetics. While recrystallization and coarsening occur post solidification, both are driven by reduction of overall interfacial energy;

notably, solute segregation occurring during solidification is one of the key contributors to the interfacial energy. Solute segregation is also necessary for phase transformations occurring during solidification in SS. In case of solute trapping at very high solidification growth rates, certain types of phase transformations, such as liquid + δ (b.c.c.) → δ (b.c.c.) + γ (f.c.c.) or liquid + γ (f.c.c.) → γ (f.c.c.) + α (b.c.c.) can be completely suppressed and the final microstructure may only contain the primary solid phase (b.c.c or f.c.c.). Depending on the fraction of secondary phases evolving during solidification, the orientation relationships (ORs), may determine the overall texture within the final component. Note that ORs are also driven by interfacial energy related phenomena; for this reason, the solute segregation and interfacial energy effects have been included within one block in Fig. 2(b). Although the segregation behavior is alloy chemistry dependent, segregation and interfacial energy related phenomena are highlighted instead of alloy chemistry in Fig. 2(b) to down select the specific factors affecting texture during F-BAM and to avoid a generic classification of such factors. Figure 3 provides an example of segregation/interfacial energy-induced changes in the phase transformation behavior in SS316L and SS316LMn alloys processed using WAAM at same parameters. Figure 3(a) and (b) correspond to the back-scattered electron (BSE) micrographs acquired from SS316L and SS316LMn, respectively. The interdendritic region for SS316L appears darker, whereas that for SS316LMn appears lighter; this indicates a variation in segregation behavior with changing chemistry. Consequently, changes in the phase transformation behavior from austenitic + ferritic in SS316L [Fig. 3(c)] to fully austenitic in SS316 LMn [Fig. 3(d)] are also evident. The resulting variation in texture from SX-like in SS316L to polycrystalline in SS316LMn is also evident and is propaedeutic for investigating the implications of segregation and/or interfacial energy related effects for crystallographic texture in more detail for F-BAM processed SS.

Having discussed the physical phenomena occurring during solidification that affect texture, we now pivot to the phenomena occurring post solidification. Thermally induced deformation can alter the as-solidified texture of SS during F-BAM processing. Invoking the fundamentals of crystal plasticity theory reveals that crystal reorientation may occur under tensile or compressive deformation [34]. Despite the prevalence of thermally induced deformation fields during F-BAM processing, studies investigating the effect of such deformation fields on the overall texture of the F-BAM processed SS are lacking. Nevertheless, deformation induced texture evolution has been widely investigated for several other thermomechanical processes, such as rolling. Considering that F-BAM is also a thermomechanical process, the effect of thermally induced deformation on texture evolution of solidified layers in F-BAM can also be investigated using similar approaches. Notably, a few works have investigated
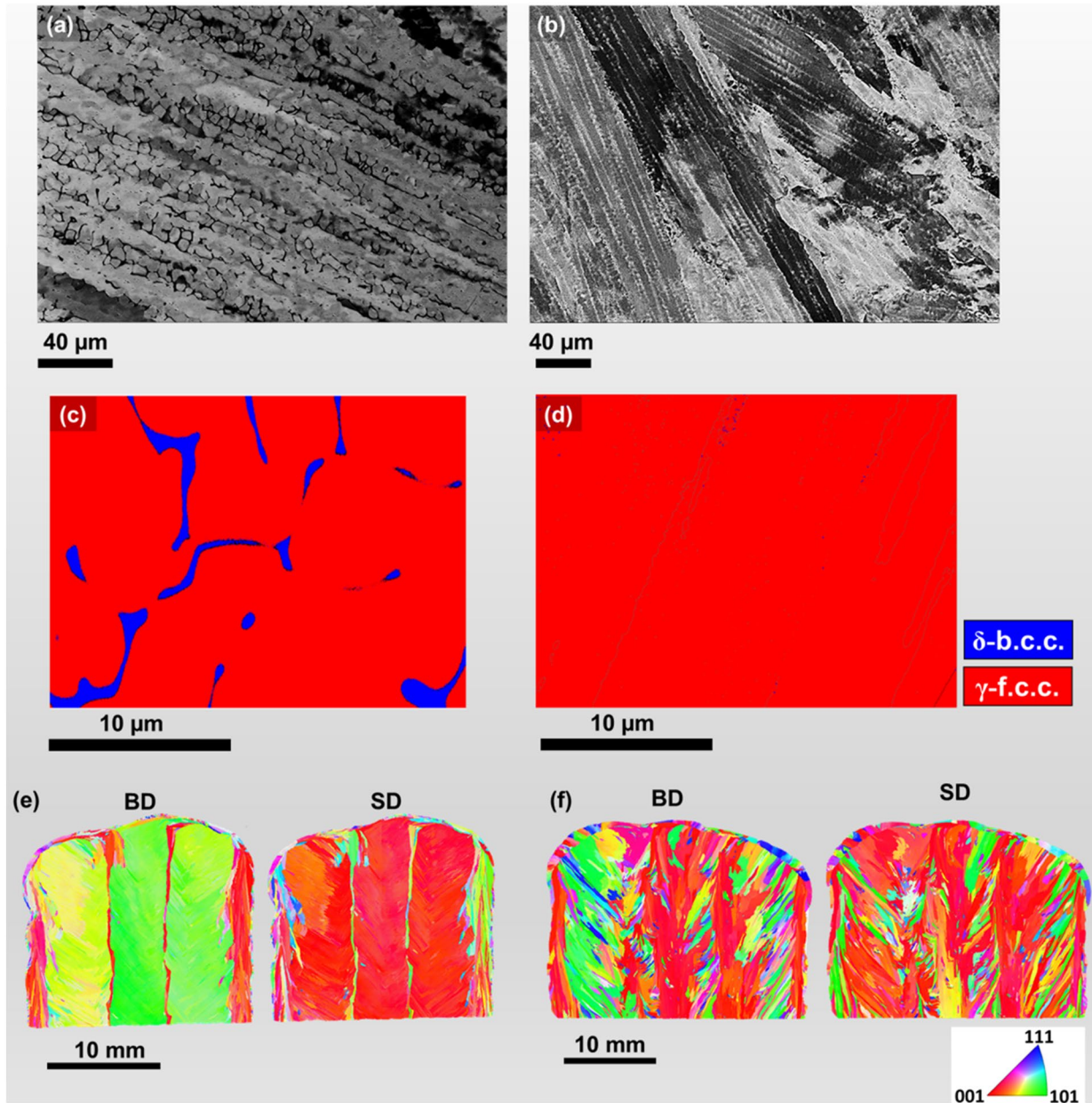
**Figure 3:** Correlating solute segregation behavior with phase transformation behavior and overall texture evolution in F-BAM processed SS. BSE micrographs for WAAM processed (a) SS316L and (b) SS316LMn. EBSD phase maps for (c) SS316L and (d) SS316LMn. EBSD IPF maps along BD and SD for (e) SS316L and (f) SS316LMn.

the effect of thermal deformation on texture evolution of F-BAM processed Ni-based alloys [2, 3]. A simple consideration of an f.c.c. crystal under tension gives that the tensile axis may rotate to a <211> orientation, whereas in compression, the compression axis of the f.c.c. crystal rotates towards a stable end orientation of <110> [34]. To demonstrate such deformation induced crystallographic reorientation in as-solidified F-BAM microstructure of SS316L, we use crystal plasticity (CP) finite element (FE) simulations. A previously presented CP model was used to study texture evolution in SS316L [35]. Single element, SX simulations

were performed for one hundred unique crystal orientations subjected to 0.2 compressive strain under uniaxial loading conditions. The as-solidified crystallographic orientations are assumed to be determined by competitive growth. Therefore, the initial orientation of each SX was determined by randomly sampling from a distribution of orientations whose <001> crystal axis is rotated counterclockwise between 30 and 40 degrees from the vertical; this is consistent with how crystals are oriented with respect to the melt pool boundaries in Fig. 3(e) and (f). As described in the illustration in Fig. 1, such competitive growth
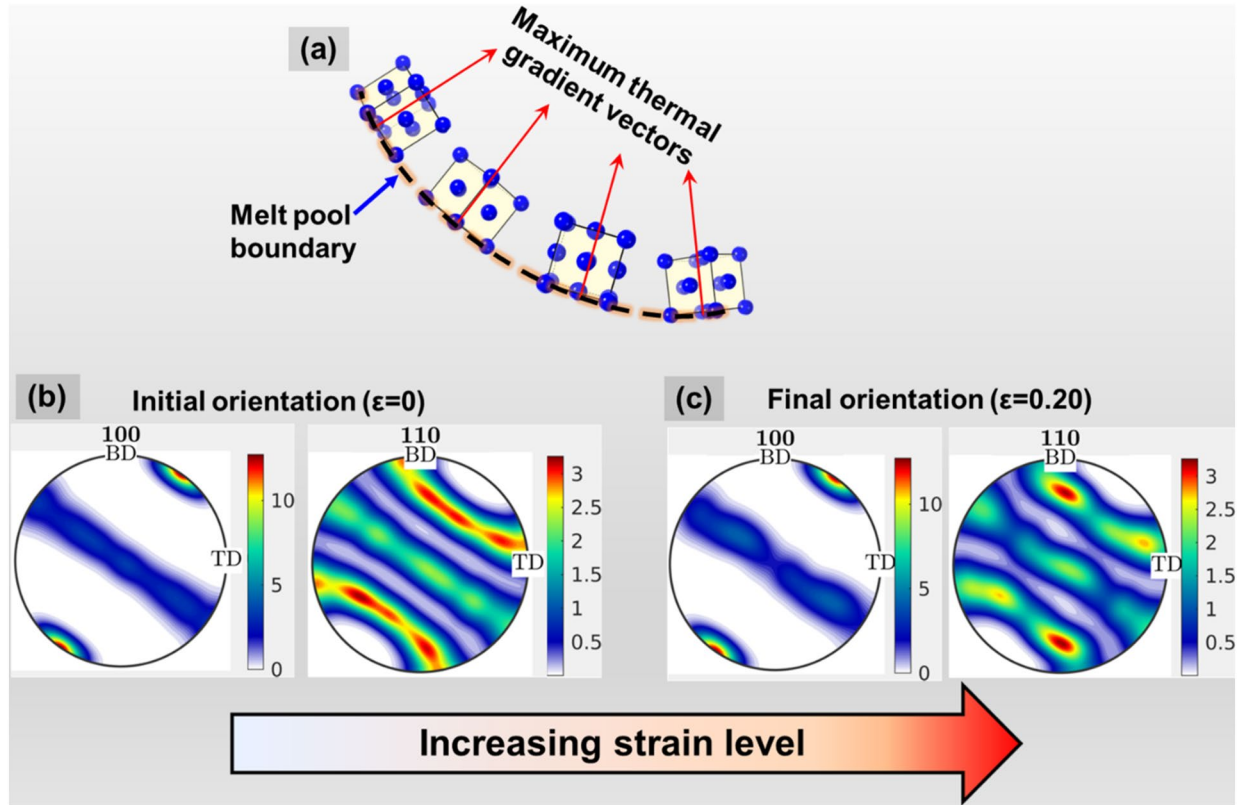
**Figure 4:** Deformation induced crystallographic reorientation as predicted by the CP FE model. (a) Illustration depicting as-solidified crystallographic orientation and (b) resulting 100 and 110 pole figures. (c) 100 and 110 pole figures of crystals depicted in (b) deformed to 0.20 strain level.

would not constrain the crystal rotation about the maximum thermal gradient vector orthogonal to the melt pool boundary. Consequently, crystals were arbitrarily rotated between 0 and 90 degrees about the maximum thermal gradient vector, i.e., the <001> crystal axis. Such crystallographic orientations are illustrated in Fig. 4(a); considering the symmetricity of the melt pool in F-BAM, the crystals in only half of the melt pool are considered in the CP FE simulations. Furthermore, the initial and final textures of the one hundred simulations are presented collectively in the form of BD-TD plane pole figures [Fig. 4(b), (c)]. Notably, with increasing strain level, the competitively grown crystals align their <011> direction along the BD. Although the boundary conditions of the simulations performed here are simplified, it is evident that thermally induced plastic deformation can play a considerable role in determining final crystallographic texture of F-BAM processed SS.

Microstructural coarsening and recrystallization may occur during F-BAM and alter the as-solidified texture. While these phenomena also arise due to thermal cycling, they differ from the deformation and phase transformation related effects of thermal cycling. Therefore, to avoid a generic classification of the factors affecting texture evolution during F-BAM, microstructural coarsening and recrystallization have been placed in a separate block in Fig. 2(b). Heat transfer from the newly deposited layer to the previously solidified layers readily occurs during F-BAM. Such heat transfer can lead to formation of heat affected zones and promotes grain coarsening in these layers [36]. Grain growth occurs at the expense of smaller and energetically less favorable grain orientations and can alter the overall solidified texture. Such phenomenon has been widely investigated for several conventionally processed SS [37–39]. Repeated heating due to thermal cycling can also result in coarsening and dissolution of second phase particles, reduced pinning force, and abnormal grain growth [37]. Note that such microstructural coarsening related phenomena are process parameter dependent, i.e., a higher energy input from the heat source will result in a larger heat affected zone, and a more pronounced effect on post solidification texture evolution. Only a limited number of studies have investigated the effect of recrystallization during F-BAM on as-solidified microstructure [40]. On the other hand, the recrystallization behavior of F-BAM processed SS and its effects on texture evolution upon post processing thermomechanical treatments have been investigated [41, 42]. Rapid cooling (from solidification)- and thermal cycle-induced deformation is known occur during F-BAM processing. Consequently, the conditions amenable for recrystallization, i.e., plastic deformation and elevated temperatures, are present during F-BAM. Therefore, depending on the component geometry (determines

thermal stresses in the component), the as-solidified microstructure, and the F-BAM process parameters, recrystallization can influence the as-solidified texture of F-BAM processed SS.

Another phenomenon that can significantly impact crystallographic texture post solidification is solid state phase transformation. Such phase transformations occur prominently during F-BAM processing of SS. In the case of displacive phase transformations, such as those seen in martensitic SS, formation of martensite is likely to result in a random or a weak texture. Such texture stems from the inherent randomness associated with selection of 24 possible variants of martensitic lattice, i.e., 24 variants of martensite lattice can form from the lattice of the parent phase [43]. Furthermore, thermal cycling related effects during F-BAM can also lead to tempering of martensitic steels and change the as-transformed or initial crystallographic texture of martensite phase [44]. The effect of such *in-process* tempering on texture will largely depend on the F-BAM process parameters, alloy chemistry and part geometry and can be subject to investigation for F-BAM processed martensitic SS. E.g., from the alloy chemistry viewpoint, for alloys with low martensite start temperatures and a high C concentration, a few implications of *in-process* tempering during F-BAM include depletion of C from martensite, recovery, and a subsequent change in as transformed texture. The formation of bainite and austenite in the heat affected zone and the implications thereof for texture have been investigated in weldments of martensitic stainless steel and ferritic martensitic steels [45, 46]. However, implications of such phase transformations for texture in F-BAM processed martensitic SS require investigation. For diffusive solid state phase transformations in SS like austenite to ferrite, texture evolution during F-BAM processing may be largely governed by orientation relationships [47]. Other diffusive solid state phase transformations that can affect the as-solidified texture include precipitation and dissolution of second phase particles. Such transformations affect the grain growth, recovery, and recrystallization kinetics, and, thus, can affect crystallographic texture.

## Prospects of grain boundary engineering with F-BAM for clean energy applications

From its advent, F-BAM has been viewed as an alternate to the conventional directional solidification processes, such as Bridgman solidification. Notably, such conventional processes are still used for manufacturing heavily textured and geometrically complex high temperature structural components. Reports of SX-like texture evolution in austenitic SS with F-BAM are promising [Fig. 3(e) and references [12, 13]], in that such texture facilitates a reduced grain boundary area, and thus, an enhanced performance of these alloys in harsh environments with good creep resistance and HE resistance. Understanding and control of physical phenomena occurring during and after solidification

as discussed in Sect. 2.1 can enable texture control and grain boundary engineering of SS with F-BAM. In this section, we discuss the prospects of achieving enhanced HE resistance in SS using such F-BAM engineered grain boundaries.

High angle grain boundaries (HAGBs) are favorable sites for hydrogen enrichment in the microstructure. Such an enrichment leads to a reduced free surface energy of grain boundaries and promotes boundary embrittlement, also called HE [8, 48]. A reduced HAGB area through texture control in F-BAM may delocalize plastic deformation from grain boundaries and reduce the HE susceptibility of the processed SS. Next, we demonstrate the implications of such grain boundary engineering with F-BAM for HE resistance. For this demonstration, we use a coupled multiphysics modeling framework that integrates CP model and the hydrogen adsorption-diffusion (HAD) model (a hydrogen transportation model) [49]. Such coupled multiphysics models can facilitate an improved understanding of effect of texture on hydrogen diffusion towards grain boundaries. The model framework assumes that when an alloy is plastically deformed, the dislocations evolve and pile-up near the grain boundaries, creating regions of lattice distortion and stress concentration zones. Such zones provide favorable conditions for the adsorption and trapping of hydrogen atoms, resulting in a local hydrogen accumulation and increase in the HE susceptibility of the alloy. Once a micro-crack is formed, the hydrogen atoms can accumulate at the tip of a propagating crack, reduce the stress required for further propagation, and promote brittle fracture. In such modeling framework, the hydrogen transportation and embrittlement are modeled at meso-scale using an integrated dislocation density-based crystal plasticity model [50] and the Sofronis and McMeeking [51] HAD model, both coupled in a temporal increment algorithm. The CP model computes the dislocation density evolution in the microstructure based on the physical interpolation of dislocation population, interaction, and annihilation process. The evolution of two types of dislocations, i.e., statistically stored dislocation (SSD) and geometrically necessary dislocation (GND), are considered in the adopted model. The rate of SSD evolution is assumed to be proportional to the slip rate on each slip system, while the GND density is computed from the Nye's dislocation density tensor which quantifies the magnitude and direction of local lattice curvature [52]. Based on the local dislocation density evolution, the slip rate on each slip plane can be computed and the combination of slip on all active slip systems determines the local plastic deformation, which gives the heterogenous deformation and stress field in the microstructure. For each time increment, the CP model informs the HAD model about the calculated stress field and dislocation density evolution. Subsequently, the HAD model predicts the diffusion and trapping of hydrogen atoms in the crystal lattice. In the HAD model, the hydrogen is assumed to diffuse through the lattice, and the high hydrostatic stresses will reduce the
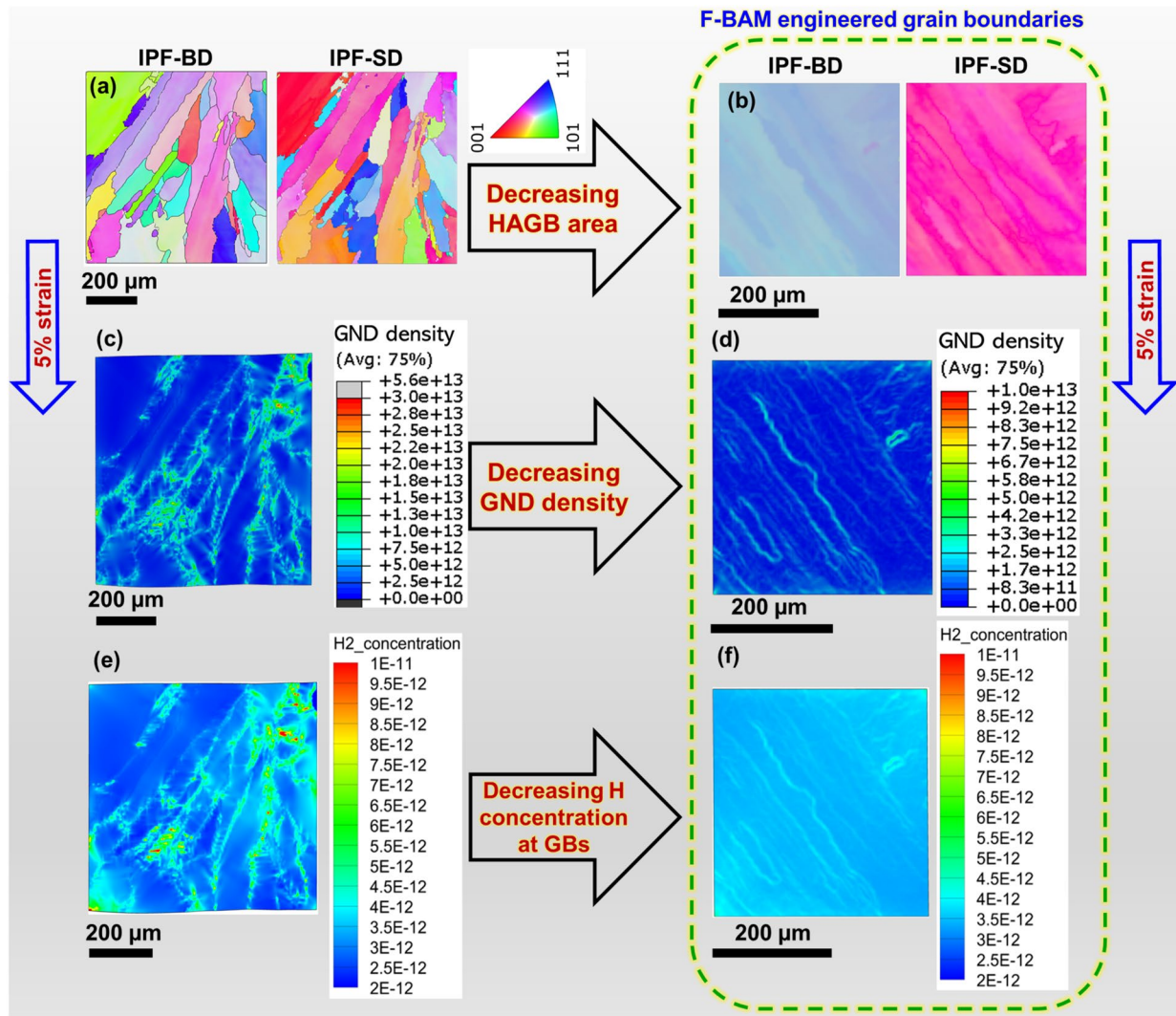
**Figure 5:** Enhanced HE resistance of F-BAM engineered grain boundaries as predicted by the CP-coupled HAD computational framework. EBSD IPF maps in BD and SD for the F-BAM processed (a) polycrystalline and (b) SX-like textured SS316L. Simulation predicted GND density distribution (in $m^{-1}$) upon 5% straining in F-BAM processed (c) polycrystalline and (d) SX-like textured SS316L. Subsequent hydrogen trapping at the grain boundaries, represented by hydrogen concentration (in $mol/m^3$) distribution maps in F-BAM processed (e) polycrystalline and (f) SX-like textured SS316L.

chemical potential and result in a flux of hydrogen from regions with compressive hydrostatic stress to regions with tensile hydrostatic stress [51]. The HAD model assumes dislocations as saturable and reversible trap sites by assuming the local number of trap sites at integration points as a function of local dislocation density [49]. The trapping of hydrogen at grain boundaries is a result of high dislocation density and stress concentration at the grain boundaries, while the grain boundary structure is not explicitly modeled. The effect of hydrogen on mechanical field, i.e., the hydrogen-induced crack initiation and propagation, is not implemented but implied by assuming an increased crack initiation probability with high local hydrogen concentration.

Figure 5 demonstrates the use of the described closed loop CP-coupled HAD model for determining the effect of texture on

HE-resistance of an F-BAM processed SS316L. The CP simulations are performed using the Abaqus commercial software, and the results are fed into an in-house HAD code to compute the hydrogen transportation. The F-BAM processed polycrystalline SS316L microstructure as depicted in the IPF maps in Fig. 5(a) and its SX-like textured counterpart with a low HAGB area as depicted in the IPF maps in Fig. 5(b) are uniaxially deformed to 5% tensile strain at room temperature and then charged in hydrogen environment (1 bar pressure) as simulated by the coupled dislocation-density based CP and HAD model [50]. The initial hydrogen concentration at the lattice sites is $2.73 \times 10^{-12}$ $mol/m^3$. Figure 5(c) and (d) show the GND density for the polycrystalline and SX-like textured SS316L, respectively, as predicted by the CP model. The simulations establish that the

polycrystalline microstructure exhibits a steeper hydrogen concentration gradient (meaning higher deformation localization) and attracts a higher concentration level of hydrogen atoms due to the abundant HAGBs [Fig. 5(e), (f)]; consequently, such microstructure is prone to the hydrogen-induced decohesion (HID) and pre-mature failure due to hydrogen-enhanced localized plasticity (HELP) mechanism [52]. On the other hand, the SX-like textured region with reduced HAGB area will exhibit a reduced propensity for grain boundary embrittlement due to lower hydrogen concentration at the boundaries as well as within the microstructure [Fig. 5(f)]. Therefore, grain boundary engineering through texture control in F-BAM combined with such closed loop coupled models will facilitate design of HE-resistant SS with F-BAM.

## Solidification behavior and perspective on high temperature mechanical behavior of F-BAM processed SS with metastable microstructure

### Thermokinetics dependent solidification modes, solidification morphologies, and hot cracking susceptibility

Solidification behavior includes attributes such as solidification modes (phase evolution during solidification), solidification morphology (planar, cellular, and dendritic), and hot cracking susceptibility (HCS) of an alloy. Common examples of solidification modes in SS include completely austenitic, FA and AF. Reports suggesting presence of fully austenitic microstructure in laser-based F-BAM processing of SS, like SS316L are common [53–55]. However, it is worth noting that a spatial variation in the solidification modes is possible due to varying thermokinetics, i.e., thermal gradients and solid–liquid interface velocity, across the build. Elaborating, the varying thermokinetics lead to variation in the solute segregation behavior across the build and subsequently lead to variation in the solidification morphology (morphology is G/R dependent). For example, planar growth is favored at the bottom of a melt pool, whereas dendritic growth becomes favorable towards the melt pool top [5]. Dendritic growth also becomes more favorable as the build height increases due to reduced thermal gradients. Such variation in solidification morphologies is a direct evidence of variation in the solute segregation behavior, thermal gradients, and growth rates across the build. As the growth rates vary, the solid–liquid interface tip temperatures of the solidifying phases can also vary across the build. At any given temperature during solidification, the phase with a higher tip undercooling or lower tip temperature is less stable as compared to the phase with a lower tip undercooling or

higher tip temperature. The tip undercooling is determined by constitutional as well as curvature undercooling. A comparison of partition coefficients of Cr in γ and Ni in δ [56] suggests that the tendency of rejection of Ni for δ phase is higher than the Cr rejection tendency of γ phase. Consequently, at high growth rates below the limit of absolute stability, i.e., where planar interface is unstable and the perturbations in the solid–liquid interface are stable, the contribution of constitutional undercooling to the total tip undercooling for δ phase may be higher than that for the γ phase [57]. Additionally, it has been shown that at high growth rates, the δ phase exhibits higher curvature undercoolings as compared to the γ phase [58]. Therefore, for solidification conditions that facilitate planar instability and are accompanied by high growth rates, the tip undercooling of δ phase may become higher than the tip undercooling for the γ phase. Such conditions may suppress the formation of δ phase from the liquid and favor the A-F mode or completely austenitic mode. Note that in F-BAM, due to high thermal gradients, the presence of high growth rates also indicates high cooling rates during solidification. As compared to the arc-based F-BAM processes, laser- and electron beam-based F-BAM processes can achieve higher cooling rates and growth rates. Therefore, an austenitic SS with a given composition may exhibit different solidification modes when processed with different F-BAM processes. Figure 6(a)–(c) demonstrate such thermokinetics-dependent variation in solidification modes for the SS316L alloy. At high growth rates, such as those available during L-PBF, the tip undercooling of the δ phase is high, and, thus, the solidification mode of the alloy can shift to completely austenitic [Fig. 6(c)] from F-A in the DED processes [Fig. 6(a), (b)]. Such variation in solidification modes may lead to variation in the HCS of the processed alloy, in that completely austenitic and A-F modes may increase the HCS of the alloy. However, the HCS in such a case would also depend on the concentration of grain boundary embrittling solute elements, such as S and P in the feedstock material for F-BAM. The segregation of such alloying elements at the cellular/dendritic boundaries may lead to a reduced free surface energy of the boundaries, and subsequently, lead to hot cracking [8, 59]. It is worth noting that although different F-BAM processes have been used to depict the varying thermokinetics in Fig. 6(a)–(c), the key takeaway is that the thermokinetics affect the solidification modes and solidification morphologies within the processed SS. Since spatial variation in thermokinetics occurs within a component irrespective of which F-BAM process is used [5], the solidification behavior can vary within a component. Therefore, the X-ray diffraction (XRD) measurements and the micrographs in Fig. 6(a)–(c) represent the most prominent solidification modes (highlighted in blue text) and morphologies (highlighted in red text) within the F-BAM processed SS, respectively.
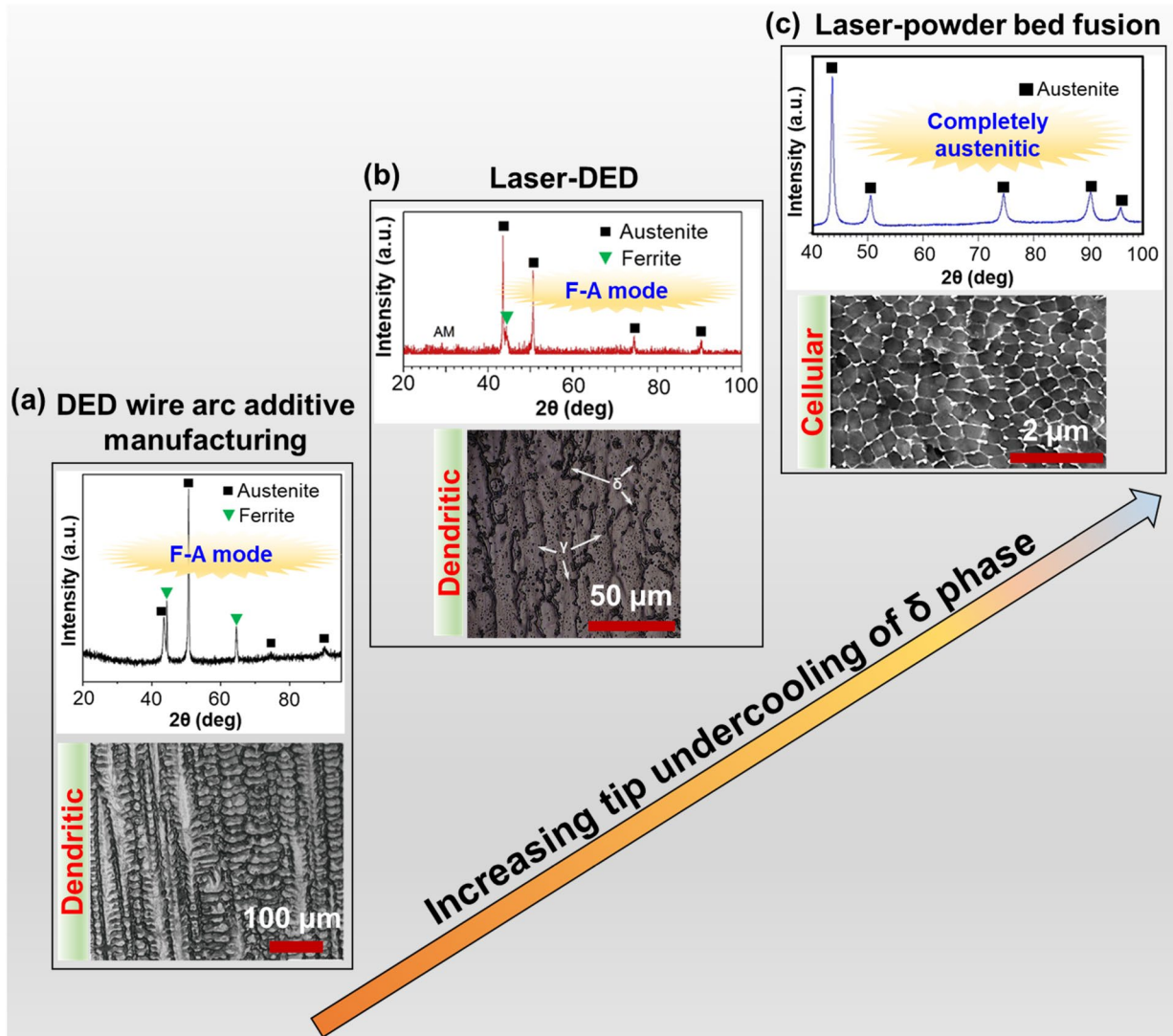
**Figure 6:** Thermokinetics-dependent solidification behavior of SS316L during F-BAM. Illustration compares the solid–liquid interface tip undercooling for the δ phase, prominently observed solidification growth morphologies, and solidification modes in (a) DED WAAM, (b) laser-DED, and (c) L-PBF process. Higher growth rates and cooling rates are available in L-PBF as compared to the DED processes, and, thus, the arrow also depicts a general trend in the growth rates and cooling rates in F-BAM. Micrographs in (a)–(c) reveal a change in the solidification morphology from dendritic in DED WAAM and laser-DED to cellular in L-PBF. XRD measurements for the DED- and L-PBF-processed SS316L demonstrate the change in solidification mode from F-A in DED to completely austenitic in L-PBF. Micrographs and XRD measurements have been adapted from [54, 60–62].

### High temperature mechanical behavior of F-BAM processed SS with metastable microstructure

Solute segregation can alter the SFE and the phase stability. Metastable microstructural features, such as retained austenite phase have been widely reported in F-BAM processed martensitic SS [25]. Such solute segregation induced alteration of alloy SFE has implications for both room and high temperature mechanical behavior. The partitioning of austenite stabilizers at localized sites within the microstructure stabilizes austenite phase at these sites. During room temperature deformation, a metastable austenite phase may undergo deformation induced phase transformation, and subsequently lead to transformation induced plasticity (TRIP) effect. TRIP often leads to a delayed dynamic recovery, a high and sustained work hardening rate, and thus, results in a high synergistic strength and ductility at room temperatures [63]. However, at elevated temperatures (below austenite start temperature), the diffusion mediated change in SFE readily occurs, i.e., austenite stabilizers can diffuse from the matrix martensitic phase towards the austenite phase and enhance the SFE of the latter. For instance, C, which is known to increase the SFE of austenite phase, can diffuse easily at elevated temperatures from supersaturated solid solution of martensite phase towards austenite and stabilize the austenite phase. Such an increase in SFE may suppress deformation

induced twinning or phase transformations and lead to embrittlement of these alloys at elevated temperatures. Also, the diffusion of C from martensite phase at elevated temperatures below the martensite start temperature leads to tempering of the martensite phase. For the arc-based large scale F-BAM processes, like WAAM, the problem of oxide formation is also prevalent. At elevated temperatures, the coarsening of oxides may prove to be detrimental to the mechanical properties. Notably, martensitic steels are commonly used for manufacturing steam turbine blades and manufacturing such geometrically complex structural components is one of the core capabilities of F-BAM processes. Considering the unique *chemistry-processing-structure-properties* relationships in F-BAM [5], very high cooling rates in F-BAM may lead to a high fraction of metastable austenite phase in the martensitic SS, such as 17–4 PH [64]. Consequently, the implications of temperature induced changes in SFE and overall microstructural attributes can be significant for F-BAM processed SS in service. Several conventionally processed austenitic and metastable steels also exhibit embrittlement at elevated temperatures [65, 66]; the temperature induced increase in SFE of low to moderate SFE steels has also been reported previously [67]. Therefore, temperature induced changes in microstructural attributes and ensuing mechanical behavior of F-BAM processed SS with metastable microstructure require detailed investigation. Design of high temperature-resistant microstructure-enabled SS with F-BAM can synergistically facilitate enhanced manufacturing efficiencies and enhanced power plants efficiencies; note that latter requires high temperature-resistant materials.

## Conclusions and outlook

Facilitating application specific and 'future-proof' manufacture of steels with fusion-based additive manufacturing processes necessitates fine tuning of microstructural attributes, like texture and solidification pathway. In this perspective article, we outline the limitations of the current approaches for understanding texture evolution in F-BAM processed steels; specifically, the current approaches predominantly focus on investigating the physical phenomena occurring only during solidification. To this end, we discuss several physical phenomena occurring during and after solidification that can determine texture evolution during F-BAM. Consideration of these phenomena can facilitate texture control and grain boundary engineering of SS with F-BAM. Furthermore, the crystal plasticity-coupled hydrogen adsorption-diffusion model establishes the hydrogen embrittlement resistance of F-BAM engineered grain boundaries.

The spatially varying thermokinetics during F-BAM often result in a variation in the solid–liquid interface tip undercoolings of the solidifying phases. Consequently, the solidification modes may vary within a component. Consideration of such variations in solidification modes is important, in that

these affect the hot cracking susceptibility and mechanical behavior of the processed SS. Manufacture of geometrically complex components, such as a turbine blades with F-BAM can be truly realized by designing an elevated temperature-resistant microstructure with F-BAM. Temperature induced changes in stacking fault energies of conventionally processed steels are well understood. Considering that several F-BAM processed martensitic SS exhibit a metastable austenite phase, investigating the temperature induced changes in SFE of F-BAM processed SS becomes imperative for designing high temperature-resistant SS with F-BAM. Considerations as outlined in this article have significant implications for grain boundary engineering with F-BAM and can lead to design of high temperature- and hydrogen embrittlement-resistant SS.

## Data availability

The datasets generated during and/or analyzed during the current study are available from the corresponding author on reasonable request.

## Declarations

**Conflict of interest** On behalf of all authors, the corresponding author states that there is no conflict of interest.

## Open Access

and indicate if changes were made. The images or other third party material in this article are included in the article's Creative Commons licence, unless indicated otherwise in a credit line to the material. If material is not included in the article's Creative Commons licence and your intended use is not permitted by statutory regulation or exceeds the permitted use, you will need to obtain permission directly from the copyright holder. To view a copy of this licence, visit http://creativecommons.org/licenses/by/4.0/.

## References

1. D.N. Lee, K.-H. Kim, Y.-G. Lee, C.-H. Choi, Factors determining crystal orientation of dendritic growth during solidification. Mater. Chem. Phys. **47**, 154 (1997)

2. J. Pistor, C. Körner, A novel mechanism to generate metallic single crystals. Sci. Rep. (2021). https://doi.org/10.1038/s41598-021-04235-2

3. A. Tabei, E. Mirkoohi, H. Garmestani, S. Liang, Modeling of texture development in additive manufacturing of Ni-based superalloys. Int. J. Adv. Manuf. Technol. **103**(1–4), 1057 (2019)

4. S. Thapliyal, R.S. Mishra, in *Quality Analysis of Additively Manufactured Metals*. ed. by J. Kadkhodapour, S. Schmauder, F. Sajadi (Elsevier, Amsterdam, 2023), pp.321–354

5. R.S. Mishra, S. Thapliyal, Design approaches for printability-performance synergy in Al alloys for laser-powder bed additive manufacturing. Mater. Des. **204**, 109640 (2021)

6. F.S.H.B. Freeman, J. Sharp, J. Xi, I. Todd, Influence of solidification cell structure on the martensitic transformation in additively manufactured steels. Addit. Manuf. **30**, 100917 (2019)

7. P. Kürnsteiner, M.B. Wilms, A. Weisheit, B. Gault, E.A. Jägle, D. Raabe, High-strength Damascus steel by additive manufacturing. Nature **582**(7813), 515 (2020)

8. S. Thapliyal, P. Agrawal, P. Agrawal, S.S. Nene, R.S. Mishra, B.A. McWilliams, K.C. Cho, Segregation engineering of grain boundaries of a metastable Fe-Mn-Co-Cr-Si high entropy alloy with laser-powder bed fusion additive manufacturing. Acta Mater. **219**, 117271 (2021)

9. N. Suutala, T. Takalo, T. Moisio, Ferritic-austenitic solidification mode in austenitic stainless steel welds. Metall. Trans. A **11**(5), 717 (1980)

10. J.C. Lippold, Solidification behavior and cracking susceptibility of pulsed-laser welds in austenitic stainless steels. Weld. J. Incl. Weld. Res. Suppl. **73**, 129 (1994)

11. L.A.I. Kestens, H. Pirgazi, Mater. Sci. Technol. (UK) **32**, 1303 (2016)

12. S.H. Sun, T. Ishimoto, K. Hagihara, Y. Tsutsumi, T. Hanawa, T. Nakano, Excellent mechanical and corrosion properties of austenitic stainless steel with a unique crystallographic lamellar microstructure via selective laser melting. Scr. Mater. **159**, 89 (2019)

13. X. Wang, J.A. Muñiz-Lerma, O. Sanchez-Mata, S.E. Atabay, M. Attarian Shandiz, M. Brochu, Single-crystalline-like stainless steel 316L with different geometries fabricated by laser powder bed fusion. Prog. Addit. Manuf. **5**(1), 41 (2020)

14. I. Karaman, H. Sehitoglu, K. Gall, Y.I. Chumlyakov, H.J. Maier, Deformation of single crystal hadfield steel by twinning and slip. Acta Mater. **48**, 1345–1359 (2000)

15. I. Gutierrez-Urrutia, S. Zaefferer, D. Raabe, The effect of grain size and grain orientation on deformation twinning in a Fe-22wt.% Mn-0.6wt.% C TWIP steel. Mater. Sci. Eng. A **527**(15), 3552 (2010)

16. M.S. Pham, B. Dovgyy, P.A. Hooper, Twinning induced plasticity in austenitic stainless steel 316L made by additive manufacturing. Mater. Sci. Eng. A **704**, 102 (2017)

17. D. Barbier, N. Gey, S. Allain, N. Bozzolo, M. Humbert, Analysis of the tensile behavior of a TWIP steel based on the texture and microstructure evolutions. Mater. Sci. Eng. A **500**(1–2), 196 (2009)

18. L. Bracke, L. Kestens, J. Penning, Direct observation of the twinning mechanism in an austenitic Fe-Mn-C steel. Scr. Mater. **61**(2), 220 (2009)

19. A. Tondro, H. Abdolvand, On the effects of texture and microstructure on hydrogen transport towards notch tips: a CPFE study. Int. J. Plast. **152**, 103234 (2022)

20. H. Zhang, J. Hu, X. Meng, Y. Sun, T. Wang, W. Lv, Q. Shi, J. Ma, D. Zhou, W. Liang, L. Zheng, Effect of deformation microstructures on hydrogen embrittlement sensitivity and failure mechanism of 304 austenitic stainless steel: the significant role of rolling temperature. J. Market. Res. **17**, 2831 (2022)

21. J. Cresko, E. Rightor, A. Carpenter, K. Peretti, N. Elliott, S. Nimbalkar, W. R. Morrow, A. Hasanbeigi, B. Hedman, S. Supekar, C. McMillan, A. Hoffmeister, A. Whitlock, T. Lgogo, J. Walzberg, C. D'Alessandro, S. Anderson, S. Atnoorkar, S. Upsani, P. King, J. Grgich, L. Ovard, R. Foist, A. Conner, M. Meshek, A. Hicks, C. Dollinger, H. Liddell, Industrial Decarbonization Roadmap (2022)

22. N. Zan, H. Ding, X. Guo, Z. Tang, W. Bleck, Effects of grain size on hydrogen embrittlement in a Fe-22Mn-0.6C TWIP steel. Int. J. Hydrogen Energy **40**(33), 10687 (2015)

23. A.J. Breen, L.T. Stephenson, B. Sun, Y. Li, O. Kasian, D. Raabe, M. Herbig, B. Gault, Solute hydrogen and deuterium observed at the near atomic scale in high-strength steel. Acta Mater. **188**, 108 (2020)

24. Y.-S. Chen, H. Lu, J. Liang, A. Rosenthal, H. Liu, G. Sneddon, I. McCarroll, Z. Zhao, W. Li, A. Guo, J.M. Cairney, Observation of hydrogen trapping at dislocations, grain boundaries, and precipitates. Science (1979) **367**(6474), 171 (2020)

25. P. Bajaj, A. Hariharan, A. Kini, P. Kürnsteiner, D. Raabe, E.A. Jägle, Steels in additive manufacturing: a review of their microstructure and properties. Mater. Sci. Eng. A **772**, 138633 (2020)

26. J.W. Christian, S. Mahajan, Deformation twinning. Prog. Mater. Sci. **39**(1), 1 (1995)

27. E. Schmid, W. Boas, Plasticity of crystals (1950)

28. M.R. Gotterbarm, A.M. Rausch, C. Körner, Fabrication of single crystals through a μ-helix grain selection process during electron beam metal additive manufacturing. Metals (Basel) **10**(3), 313 (2020)

29. P. Fernandez-Zelaia, M.M. Kirka, A.M. Rossy, Y. Lee, S.N. Dryepondt, Nickel-based superalloy single crystals fabricated via electron beam melting. Acta Mater. **216**, 117133 (2021)

30. S. Thapliyal, S. Shukla, L. Zhou, H. Hyer, P. Agrawal, P. Agrawal, M. Komarasamy, Y. Sohn, R.S. Mishra, Design of heterogeneous structured Al alloys with wide processing window for laser-powder bed fusion additive manufacturing. Addit. Manuf. **42**, 102002 (2021)

31. H. Tao, L.U. Deyang, Z. Yaohe, Diffusion-convection effects on constrained dendritic growth in dilute alloys? Acta Astron. **17**, 997 (1988)

32. D.N. Lee, Orientations of dendritic growth during solidification. Met. Mater. Int. **23**(2), 320 (2017)

33. K. Dragnevski, A.M. Mullis, D.J. Walker, R.F. Cochrane, Mechanical deformation of dendrites by fluid flow during the solidification of undercooled melts. Acta Mater. **50**, 3743 (2002)

34. W.F. Hosford, *Mechanical Behavior of Materials*, 2nd edn. (Cambridge University Press, New York, 2010)

35. C.A. Bronkhorst, J.R. Mayeur, V. Livescu, R. Pokharel, D.W. Brown, G.T.G. Iii, Structural representation of additively manufactured 316l austenitic stainless steel. Int. J. Plast. **118**, 80–96 (2019)

36. A. Dhal, S. Thapliyal, S. Gaddam, P. Agrawal, R.S. Mishra, Multiscale hierarchical and heterogeneous mechanical response of additively manufactured novel Al alloy investigated by high-resolution nanoindentation mapping. Sci. Rep. **12**(1), 18344 (2022)

37. M. Shirdel, H. Mirzadeh, M. Habibi Parsa, Metall. Mater. Trans. A Phys. Metall. Mater. Sci. **45**, 5185–5193 (2014)

38. W. Huang, S. Yuan, L. Chai, L. Jiang, H. Liu, F. Wang, D. Wang, J. Wang, Development of grain boundary character distribution in medium-strained 316L stainless steel during annealing. Met. Mater. Int. **25**(2), 364 (2019)

39. S. Tokita, H. Kokawa, Y.S. Sato, H.T. Fujii, In situ EBSD observation of grain boundary character distribution evolution during thermomechanical process used for grain boundary engineering of 304 austenitic stainless steel. Mater. Charact. **131**, 31 (2017)

40. E. Mirkoohi, D. Li, H. Garmestani, S.Y. Liang, Residual stress modeling considering microstructure evolution in metal additive manufacturing. J. Manuf. Process. **68**, 383 (2021)

41. S. Gao, Z. Hu, M. Duchamp, P.S.S.R. Krishnan, S. Tekumalla, X. Song, M. Seita, Recrystallization-based grain boundary engineering of 316L stainless steel produced via selective laser melting. Acta Mater. **200**, 366 (2020)

42. T.R. Smith, J.D. Sugar, J.M. Schoenung, C. San Marchi, Anomalous annealing response of directed energy deposited type 304L austenitic stainless steel. JOM **70**(3), 358 (2018)

43. H.K.D.H. Bhadeshia, Problems in the calculation of transformation texture in steels. ISIJ Int. **50**(11), 1517 (2010)

44. M.R. Suresh, I. Samajdar, A. Ingle, N.B. Ballal, P.K. Rao, P.P. Sinha, Structure-property changes during hardening and tempering of new ultra high strength medium carbon low alloy steel. Ironmak. Steelmak. **30**(5), 379 (2003)

45. J.B. Lévesque, J. Lanteigne, H. Champliaud, D. Paquet, Modeling solid-state phase transformations of 13Cr-4Ni steels in welding heat-affected zone. Metall. Mater. Trans. A Phys. Metall. Mater. Sci. **51**(3), 1208 (2020)

46. Y. Wang, R. Kannan, L. Li, Characterization of as-welded microstructure of heat-affected zone in modified 9Cr-1Mo-V-Nb steel weldment. Mater. Charact. **118**, 225 (2016)

47. N. Sayyar, V. Hansen, W.M. Tucho, M.W. Minde, Directed laser deposition of super duplex stainless steel: microstructure, texture evolution, and mechanical properties. Heliyon **9**(4), e15144 (2023)

48. X. Zhou, W.A. Curtin, First principles study of the effect of hydrogen in austenitic stainless steels and high entropy alloys. Acta Mater. **200**, 932 (2020)

49. A. Hussein, A.H.M. Krom, P. Dey, G.K. Sunnardianto, O.A. Moultos, C.L. Walters, The effect of hydrogen content and yield strength on the distribution of hydrogen in steel: a diffusion coupled micromechanical FEM study. Acta Mater. **209**, 116799 (2021)

50. J. Cheng, X. Hu, M. Kirka, A cycle-jump acceleration method for the crystal plasticity simulation of high cycle fatigue of the metallic microstructure. Int. J. Fatigue **165**, 107185 (2022)

51. P. Sofronis, R.M. McMeeking, Numerical analysis of hydrogen transport near a blunting crack tip. J. Mech. Phys. Solids **37**(3), 317 (1989)

52. O. Barrera, D. Bombac, Y. Chen, T.D. Daff, E. Galindo-Nava, P. Gong, D. Haley, R. Horton, I. Katzarov, J.R. Kermode, C. Liverani, M. Stopher, F. Sweeney, Understanding and mitigating hydrogen embrittlement of steels: a review of experimental, modelling and design progress from atomistic to continuum. J. Mater. Sci. **53**(9), 6251 (2018)

53. E. Liverani, S. Toschi, L. Ceschini, A. Fortunato, Effect of selective laser melting (SLM) process parameters on microstructure and mechanical properties of 316L austenitic stainless steel. J. Mater. Process. Technol. **249**, 255 (2017)

54. Y. Zhong, L. Liu, S. Wikman, D. Cui, Z. Shen, Intragranular cellular segregation network structure strengthening 316L stainless steel prepared by selective laser melting. J. Nucl. Mater. **470**, 170 (2016)

55. D.R. Feenstra, V. Cruz, X. Gao, A. Molotnikov, N. Birbilis, Effect of build height on the properties of large format stainless steel 316L fabricated via directed energy deposition. Addit. Manuf. **34**, 101205 (2020)

56. H.W. Kerr, W. Kurz, Solidification of peritectic alloys. Int. Mater. Rev. **41**(4), 129 (1996)

57. S.S. Babu, J.W. Elmer, S.A. David, M.A. Quintana, In situ observations of non-equilibrium austenite formation during weld solidification of an Fe-C-Al-Mn low-alloy steel. Proc. R. Soc. A **458**(2020), 811 (2002)

58. S. Fukumoto, W. Kurz, Prediction of the δ to γ during laser treatment transition in austenitic stainless steels during laser treatment. ISIJ Int. **38**, 71–77 (1998)

59. M. Rappaz, A. Jacot, W.J. Boettinger, Last-stage solidification of alloys: Theoretical model of dendrite-arm and grain coalescence. Metall. Mater. Trans. A Phys. Metall. Mater. Sci. **34A**(3), 467 (2003)

60. B. Xie, J. Xue, X. Ren, Wire arc deposition additive manufacturing and experimental study of 316l stainless steel by cmt + p process. Metals (Basel) **10**(11), 1 (2020)

61. J. Nie, L. Wei, Y. Jiang, Q. Li, H. Luo, Corrosion mechanism of additively manufactured 316 L stainless steel in 3.5 wt.% NaCl solution. Mater. Today Commun. **26**, 101648 (2021)

62. F. Weng, S. Gao, J. Jiang, J.J. Wang, P. Guo, A novel strategy to fabricate thin 316L stainless steel rods by continuous directed energy deposition in Z direction. Addit. Manuf. **27**, 474 (2019)

63. S. Thapliyal, S.S. Nene, P. Agrawal, T. Wang, C. Morphew, R.S. Mishra, B.A. McWilliams, K. Cho, Damage-tolerant high entropy alloy with high corrosion resistance by laser powder bed fusion additive manufacturing. Addit. Manuf. **36**, 101455 (2020)

64. L. Facchini, N. Vicente, I. Lonardelli, E. Magalini, P. Robotti, M. Alberto, Metastable austenite in 17–4 precipitation-hardening stainless steel produced by selective laser melting. Adv. Eng. Mater. **12**(3), 184 (2010)

65. D. Molnár, X. Sun, S. Lu, W. Li, G. Engberg, L. Vitos, Effect of temperature on the stacking fault energy and deformation behaviour in 316L austenitic stainless steel. Mater. Sci. Eng. A **759**, 490 (2019)

66. L. Wang, J.G. Speer, Quenching and partitioning steel heat treatment. Metallogr. Microstruct. Anal. **2**(4), 268 (2013)

67. Y.K. Lee, S.J. Lee, J. Han, Critical assessment 19: stacking fault energies of austenitic steels. Mater. Sci. Technol. (UK) **32**(1), 1 (2016)